Received: 13 July 2020 | Revised: 19 December 2020 | Accepted: 11 January 2021

DOI: 10.1002/mrm.28713

FULL PAPER

Magnetic Resonance in Medicine

Similarity-driven multi-dimensional binning algorithm (SIMBA) for free-running motion-suppressed whole-heart MRA

John Heerfordt[1,2] | Kevin K. Whitehead[3] | Jessica A. M. Bastiaansen[1] | Lorenzo Di Sopra[1] | Christopher W. Roy[1] | Jérôme Yerly[1,4] | Bastien Milani[1] | Mark A. Fogel[3] | Matthias Stuber[1,4] | Davide Piccini[1,2]

[1]Department of Diagnostic and Interventional Radiology, Lausanne University Hospital and University of Lausanne, Lausanne, Switzerland

[2]Advanced Clinical Imaging Technology, Siemens Healthcare AG, Lausanne, Switzerland

[3]Division of Cardiology, Department of Pediatrics, The Children's Hospital of Philadelphia, University of Pennsylvania Perelman School of Medicine, Philadelphia, Pennsylvania, USA

[4]Center for Biomedical Imaging, Lausanne, Switzerland

Correspondence
Davide Piccini, Center for Biomedical Imaging, Centre Hospitalier Universitaire Vaudois, Rue du Bugnon 46, BH 7.82, 1011 Lausanne, Switzerland.
Email: piccinidavide@gmail.com

Funding information
This work was supported by two different grants from the Schweizerischer Nationalfonds zur Förderung der Wissenschaftlichen Forschung (173129 and PZ00P3_167871), Swiss Heart Foundation (FF18054), and Emma Muschamp Foundation

Purpose: Whole-heart MRA techniques typically target predetermined motion states, address cardiac and respiratory dynamics independently, and require either complex planning or computationally demanding reconstructions. In contrast, we developed a fast data-driven reconstruction algorithm with minimal physiological assumptions and compatibility with ungated free-running sequences.

Theory and Methods: We propose a similarity-driven multi-dimensional binning algorithm (SIMBA) that clusters continuously acquired k-space data to find a motion-consistent subset for whole-heart MRA reconstruction. Free-running 3D radial data sets from 12 non-contrast-enhanced scans of healthy volunteers and six ferumoxytol-enhanced scans of pediatric cardiac patients were reconstructed with non-motion-suppressed regridding of all the acquired data ("All Data"), with SIMBA, and with a previously published free-running framework (FRF) that uses cardiac and respiratory self-gating and compressed sensing. Images were compared for blood–myocardium sharpness and contrast ratio, visibility of coronary artery ostia, and right coronary artery sharpness.

Results: Both the 20-second SIMBA reconstruction and FRF provided significantly higher blood–myocardium sharpness than All Data in both patients and volunteers ($P < .05$). The SIMBA reconstruction provided significantly sharper blood–myocardium interfaces than FRF in volunteers ($P < .001$) and higher blood–myocardium contrast ratio than All Data and FRF, both in volunteers and patients ($P < .05$). Significantly more ostia could be visualized with both SIMBA (31 of 36) and FRF (34 of 36) than with All Data (4 of 36) ($P < .001$). Inferior right coronary artery sharpness using SIMBA versus FRF was observed (volunteers: SIMBA 36.1 ± 8.1%, FRF 40.4 ± 8.9%; patients: SIMBA 35.9 ± 7.7%, FRF 40.3 ± 6.1%, $P =$ *not significant*).

Conclusion: The SIMBA technique enabled a fast, data-driven reconstruction of free-running whole-heart MRA with image quality superior to All Data and similar to the more time-consuming FRF reconstruction.

KEYWORDS

3D radial, clustering, ferumoxytol, free-running, noncontrast MRA, whole heart

1 | INTRODUCTION

High-resolution MRI of the whole heart and great vessels plays an important role in the assessment of congenital heart disease,[1] including malformations at the coronary origins[2] and anatomical measurements of the thoracic vasculature.[3] It also allows for the examination of coronary artery stenoses[4,5] and for planning of subsequent scans using highly detailed 3D images.[6] To obtain motion-suppressed volumetric anatomical images, a specific motion state of the heart (e.g., the diastolic cardiac resting phase at end-expiration) is generally targeted during the data acquisition. In state-of-the-art approaches, cardiac and respiratory motion components are commonly regarded as separate entities for which different motion-suppression strategies are applied. Artifacts originating from cardiac motion can be minimized by triggering the acquisition to specific cardiac phases using an external electrocardiogram (ECG) signal. The drawbacks of this approach include the placement of the electrodes, the requirement for careful planning of appropriate trigger delays and acquisition windows, the fact that ECG signals are unreliable in the MRI environment, and that the RR interval may vary during the acquisition.[7] In turn, respiratory-motion artifacts can be minimized using breath-holds or by gating the data acquisition to predefined respiratory levels with respiratory bellows[8,9] or with diaphragmatic navigator echoes.[10] However, while the latter also requires dedicated planning and is both time-inefficient and sensitive to variations in the breathing pattern,[11] the former implies a compromise in resolution and spatial coverage, especially in uncooperative patients.

Whole-heart MRA approaches that address these shortcomings have been proposed. Examples include avoiding ECGs by using cardiac self-gating,[12,13] avoiding diaphragmatic navigators by performing respiratory motion correction based on one-dimensional (1D) projections[14] or image navigators,[15] and using physiological self-gating signals to bin the data into different motion states, to resolve motion.[12,13,16,17] Free-running whole-heart pulse sequences[12,18] that acquire data continuously, regardless of the ongoing physiological motion, allow for simplified planning and become particularly powerful when combined with binning, as cine images can be obtained.[12,13,17,18] Recently, a fully automated free-running framework (FRF), consisting of continuous acquisition, full self-gating, and cardiac and respiratory motion-resolved reconstruction, was proposed.[13]

All of these methodologies hinge on targeting specific motion states by extracting and processing cardiac and respiratory motion independently, either prospectively during the acquisition or retrospectively as part of the reconstruction routine. This builds on the assumption that data from such targeted motion states must intrinsically have a high degree of motion consistency, thus resulting in images with a low level of motion artifacts. Nonetheless, there remain a whole range of challenges. For example, when a predetermined motion state is targeted, the diastolic resting phase at end-expiration is often assumed to be optimal. This may not always be the case, as in certain subjects end-systole[19] and other respiratory levels than end-expiration[20] may be more adequate. An additional complicating factor is that the diastolic cardiac resting phase may be affected by temporal changes in the heart rate during a scan, which ideally should be accounted for by the imaging technique.[21] Cardiac and respiratory self-gating methods typically rely on explicit assumptions regarding expected frequency ranges for cardiac and respiratory motion.[12,13] Lastly, motion-resolved compressed-sensing reconstructions may last several hours.[17] With all of this in mind, we propose to reverse the underlying assumptions. Instead of regarding cardiac and respiratory motion components as separate entities and targeting specific motion states, we leverage intrinsic similarities in the acquired data to find a subset with a high level of motion consistency. If such a subset can be obtained, it should enable rapid and straightforward reconstruction of a motion-suppressed image, provided that sufficient k-space uniformity is maintained.

To that end, a novel fast similarity-based whole-heart image reconstruction method is proposed, described, validated, and tested in this work. On the acquisition side, existing free-running data collection strategies[12,13,18] that offer uniform coverage of k-space over time (by reordering schemes based on the golden angle[22,23]) are used. On the reconstruction side, the acquired MRI data are clustered based on their inherent similarities, to identify motion-consistent subsets that can be used for reconstructing motion-suppressed static whole-heart MRA. Consequently, there is no need to explicitly differentiate motion sources from one another, nor use iterative reconstruction, provided that the subsets are sufficiently populated. The objectives of this study were to investigate (1) whether

this similarity-driven reconstruction results in whole-heart images with sharp anatomical features, including coronary arteries as a surrogate endpoint for motion consistency, and (2) whether data that cluster together intrinsically originate from well-defined phases of the cardiac and respiratory cycles. Preliminary results from this work have been presented in abstract form.[24]

2 | THEORY

2.1 | Background

Consider the task of reconstructing a sharp static 3D anatomical image of the heart using MR data obtained with an ungated and untriggered free-running acquisition, in which the scan time was long enough for considerable cardiac and respiratory motion to occur. Without any motion-suppression strategy, it is clearly suboptimal to reconstruct all of the acquired data into one single image, as this would be heavily degraded by motion artifacts.[25] Therefore, we seek to identify a subset of the collected data that was acquired during a similar, unspecified anatomical motion state and that can consequently be used for reconstructing an image without apparent motion artifacts.

2.2 | Similarity-based clustering

The similarity-driven multidimensional binning algorithm (SIMBA) proposed in this work involves grouping the acquired MR data into k disjoint subsets/clusters $\mathbf{C} = \{C_1, C_2, \ldots, C_k\}$ that are populated based on the similarity of a total number of T reference data vectors $\mathbf{s}_1, \mathbf{s}_2, \ldots, \mathbf{s}_T$, $\mathbf{s}_i \in \mathbb{R}^N$. These vectors are constructed from certain MRI data, intrinsically modulated by physiological motion, that are acquired throughout the whole free-running acquisition at regularly spaced time points $t_1, t_2, \ldots, t_T$ (Figure 1). Candidates for such reference data can be found in the self-gating literature, such as the magnitude of the k-space center coefficient,[26] 1D projection images in the superior–inferior (SI) direction[14] or a vectorized representation of an image navigator.[27] Hence, if the reference-data vectors from some of the time points show a high degree of similarity, it may be inferred that the heart may have been at a similar position and contractile state at those instances. Note that $t_{i+1} - t_i$ should be short enough that it can be assumed that very little organ motion occurred during that period.

For the concrete assessment of similarity, let us create a matrix $\mathbf{S} \in \mathbb{R}^{N \times T}$ by concatenating the T reference data vectors $\mathbf{s}_1, \mathbf{s}_2, \ldots, \mathbf{s}_T$ with N elements each according to their temporal order of acquisition. Thus, each column of $\mathbf{S}$ corresponds to a reference data vector. If a free-running sequence repeatedly acquires the same k-space line or sample at the time points $t_1, t_2, \ldots, t_T$, such a matrix can easily be created by letting these measurements serve as reference data. Once $\mathbf{S}$ has been populated, the task at hand is to group its columns with reference data vectors (ie, points in an N-dimensional space) into the different clusters $C_1, C_2, \ldots, C_k$ using an appropriate clustering technique and a distance metric. If the reference data vectors are of high dimensionality, dimensionality reduction before the clustering step may be beneficial.[28] In this work, we use k-means,[29] meaning that the data points are assigned to clusters in a way that minimizes the sum of the intracluster sum-of-squares distances:

$$\underset{\mathbf{C}}{\operatorname{argmin}} \sum_{j=1}^{k} \sum_{\mathbf{s}_i \in C_j} \left\| \mathbf{s}_i - \mu_j \right\|^2 \tag{1}$$

where $\mathbf{s}_i$ is the ith column of $\mathbf{S}$, and μ_j is the centroid of the jth cluster that corresponds to the average of all data points assigned to the cluster. This optimization problem (Equation 1) is normally solved in an iterative fashion that is sensitive to initial conditions, which is why ascertaining a good spread of the initial centroids with the k-means^{++} algorithm[30] may be advantageous.

2.3 | From clusters to images

After assigning the reference data obtained at the time points $t_1, t_2, \ldots, t_T$ to different clusters, the remaining k-space data have to be assigned as well. For interleaved acquisitions in which one reference data vector is obtained per interleaf, this is easily accomplished by assigning all the data within one interleaf to the same cluster as its reference data. Alternatively, one can imagine assigning all of the data acquired within a certain temporal window around each time point to the same cluster as the corresponding reference data vector. Provided that the different clusters contain motion-consistent data with a relatively uniform k-space distribution, standard image reconstruction of the data in such a cluster should result in an image with a low level of both motion-related and sampling-related artifacts.

3 | METHODS

3.1 | The SIMBA reconstruction for free-running 3D radial whole-heart imaging

Here, we describe and validate an implementation of SIMBA designed for ungated free-running sequences with

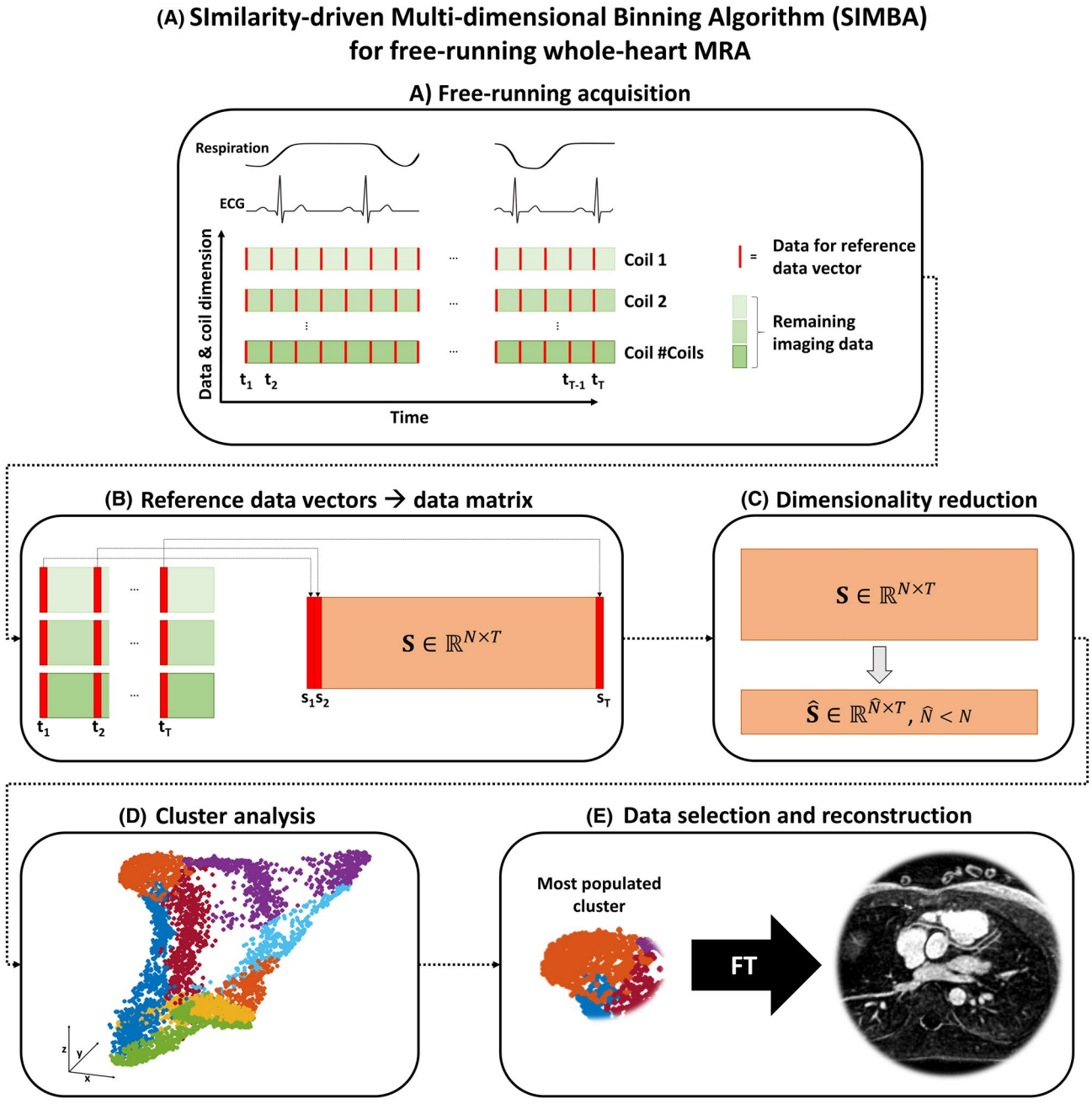

FIGURE 1 Overview of the similarity-driven multidimensional binning algorithm (SIMBA) for free-running whole-heart MRA. A, Whole-heart MRA data are acquired using an ungated, untriggered free-running sequence with regular sampling of reference data (ie, imaging data that are modulated by physiological motion). B, Subsequently, the reference data vectors s_1, s_2, …, s_T are constructed using the reference data sampled at the time points t_1, t_2, …, t_T from a number of selected coil elements. The reference data vectors are concatenated in chronological order into the data matrix **S**. C, The number of rows of **S** is reduced to facilitate the subsequent clustering of the data matrix's columns. D, Cluster analysis is performed on the dimensionality-reduced reference data vectors (ie, the columns of $\hat{\mathbf{S}}$). By design, the reference data vectors are modulated by physiological motion, which means that a cluster of similar vectors is expected to correspond to data that were acquired during a similar anatomical state. E, The imaging data acquired in proximity (in time) to the reference data vectors of the most populated cluster are extracted and Fourier-transformed (FT) into a 3D image. Abbreviation: ECG, electrocardiogram

interleaved 3D radial sampling patterns.[12,18] Such acquisitions are suitable for SIMBA, because they make use of a golden-angle increment, ensuring that a random subset of interleaves provides approximately uniform k-space sampling, and acquire an SI readout every interleaf. Here, 1D Fourier transforms of such SI readouts are used for creating the reference data vectors that form the data matrix **S** in the SIMBA clustering (one SI readout per interleaf is

acquired). Given a free-running acquisition of the heart consisting of a total number of $N_{interleaves} \in \mathbb{N}$ radial interleaves, our goal is to group these interleaves into k disjoint clusters C_1, C_2,…, C_k, $k << N_{interleaves}$ using reference data vectors created from the SI projections from the time points t_1, t_2, …,$t_{N_{interleaves}}$. Each reference data vector is a concatenation of 1D gradients (with $N_{samples}$ elements per gradient) of the corresponding SI projections from $N_{coil} = 4$ fixed and centrally located chest surface-coil elements. Gradients of the projections, computed as first-order forward differences in the readout direction, are used to reduce the dependency on the sequence contrast due to the intrinsic normalization and to highlight interfaces such as the lung–liver interface. The main steps of this SIMBA implementation are described subsequently (Figure 1):

1. Data acquisition with an interleaved free-running 3D radial sequence with regularly acquired SI readouts.
2. 1D gradients of the magnitude SI projections from the selected chest-coil elements are computed. Each gradient vector is standardized to have a mean value of zero and a variance of one before concatenating the gradients into reference data vectors for the different interleaves. Subsequently, these reference data vectors are organized into the data matrix $\mathbf{S} \in \mathbb{R}^{(N_{coil} \times N_{samples}) \times N_{interleaves}}$.
3. Dimensionality reduction with principal component analysis is used to reduce the dimensionality of $\mathbf{S}$. The $N_{PC} = 20$ principal components that explain the most variance are extracted by applying principal component analysis along the interleaf direction. The choice of $N_{PC} = 20$ was empirically made as a trade-off between explanatory power and restricting the dimensionality. The first principal component is discarded because of its marginal impact on the subsequent clustering (due to its small SD), and the remaining $N_{PC}1-1 = 19$ principal components are used to create the low-dimensional data matrix $\hat{\mathbf{S}} \in \mathbb{R}^{(N_{PC}-1) \times N_{interleaves}}$.
4. Given this low-dimensional representation $\hat{\mathbf{s}}_1, \hat{\mathbf{s}}_2, \ldots, \hat{\mathbf{s}}_{N_{interleaves}}$, $\hat{\mathbf{s}} \in \mathbb{R}^{N_{PC}1-1}$ of the different interleaves ($\hat{\mathbf{s}}_j$ denotes the jth column of $\hat{\mathbf{S}}$), k-means clustering is used to group the interleaves into the k disjoint clusters C_1, C_2, …, C_k. The number of clusters is determined based on existing knowledge from triggered 3D radial coronary MRA, namely, that 12 000-15 000 readouts are adequate for reconstructing a whole-heart volume with isotropic millimetric spatial resolution[31,32] without the need for an expensive iterative reconstruction approach. Seeking to maintain approximately that amount of data in the most populated cluster $C_{largest}$, an automated search procedure was developed, which picks k in the range of 10-14 based on which particular k minimizes the average distance between the centroid and the data points of the most populated cluster:

$$\underset{k \in \{10,11,..,14\}}{\operatorname{argmin}} = \frac{1}{\left|C_{largest}\right|} \sum_{\hat{\mathbf{s}} \in C_{largest}} \left\| \mu_{largest,k} - \hat{\mathbf{s}} \right\|_2, \quad (2)$$

where $\mu_{largest,k}$ denotes the centroid of the most populated cluster after performing k-means clustering with k clusters, and its cardinality $\left|C_{largest}\right|$ denotes the number of interleaves in that cluster.

5. Finally, the data corresponding to the interleaves of the most populated cluster $C_{largest}$ are extracted, and a standard non-Cartesian reconstruction is performed, consisting of density compensation, nonuniform fast Fourier transform[33] (regridding to a Cartesian grid, inverse Fourier transformation, and roll-off correction[34]), and sum-of-squares coil combination.

3.2 | Data acquisition

In this internal review board–approved study, the SIMBA reconstruction was evaluated using free-running 3D radial data sets acquired in two different cohorts of human subjects: 12 healthy volunteers (28 ± 4 years, 9 male) were scanned with a fat-saturated balanced SSFP[18] sequence, and 6 pediatric congenital heart disease patients (6 ± 4 years, 4 male) underwent imaging with a contrast-enhanced gradient-echo sequence under respiratory ventilation after administration of ferumoxytol.[35] Volunteers and patients were imaged on 1.5T MAGNETOM Aera and Avanto^{fit} clinical scanners (Siemens Healthcare, Erlangen, Germany), respectively. All acquisitions consisted of 5749 interleaves with 22 readouts each following a prototype 3D radial phyllotaxis trajectory.[36] Additional acquisition parameters are found in Table 1. The ECG was recorded solely as a reference for retrospective analysis of SIMBA's data selection.

3.3 | Image reconstruction

Each of the free-running data sets was reconstructed with SIMBA and two reference techniques: a conventional 3D gridding reconstruction[33] of all the collected radial data without motion correction ("All Data") and a fully self-gated cardiac and respiratory motion-resolved compressed-sensing reconstruction that recently was reported as part of FRF.[13] The motion-resolved FRF reconstructions used four respiratory phases and a temporal cardiac resolution of 50 ms. For all comparisons, end-expiratory FRF images from a cardiac resting phase were used. In addition, the reconstruction times were measured. The noniterative All Data and SIMBA reconstructions can be performed on a standard computer, whereas powerful hardware is required for the iterative motion-resolved compressed-sensing reconstruction algorithm XD-GRASP[17,37] used in FRF.

TABLE 1 Data sets used in the study

Parameter	FS-bSSFP volunteer scans	CE-GRE patient scans
Cohort	12 healthy adult volunteers	6 pediatric cardiac patients
Contrast agent	None	Ferumoxytol (4 mg/kg)
Scanner	1.5T MAGNETOM Aera	1.5T MAGNETOM Avanto^{fit}
Sequence	Fat-saturated bSSFP with 10 ramp-up pulses	Spoiled GRE
Sampling scheme	3D radial spiral phyllotaxis	
Number of spokes	126 478 (5749 interleaves with 22 spokes)	
FOV (mm^3)	220^3	180^3-220^3
Acquired resolution (mm^3)	1.1^3	0.9^3-1.1^3
TE/TR (ms)	1.56/3.12	1.55-1.74/3.34-3.65
RF excitation angle	90°	15°
Receiver bandwidth (Hz/pixel)	898	1000-1085
Acquisition time (mm:ss)	14:17	7:03-7:42

3.4 | Analysis of image quality

To study our first objective, image quality was evaluated using different metrics. The sharpness of the blood–myocardium interface was measured for all three reconstruction types. This was done by fitting parametrized sigmoid functions to the blood–myocardium interface of the left ventricle, using a parametrization in which the value of the slope parameter describing the sigmoid depends on the interface's sharpness.[38] These measurements were performed in coronal reformats at the same anatomical position for all of the reconstruction types. The final sharpness value for each image type and subject was obtained as the average slope parameter of six fitted sigmoid functions, three oriented in the medial-lateral and three in the SI direction. The blood–myocardium contrast ratio (CR) was quantified by comparing average signal intensities in regions of interest (one in the left ventricle's blood pool and one in the septal wall of the myocardium) in a midmyocardial axial reformat, computed as $\mathrm{CR} = \frac{\mathrm{Signal}_{blood} - \mathrm{Signal}_{myocardium}}{\mathrm{Signal}_{myocardium}}$. Measurements of blood SNR and blood–myocardium contrast-to-noise ratio (CNR) were only performed for All Data and SIMBA, as the use of parallel imaging and compressed sensing impacts the background noise distribution in the FRF images. The normalization factors in Dietrich et al.[39] were used to correct for the noise distribution in the magnitude images.

Furthermore, the ostia of the right coronary artery (RCA) and the left main (LM) were categorized as either visible or nonvisible in a consensus reading by 2 authors (J.H. and D.P. with 3 and 10 years of experience in coronary MRA, respectively). Subsequently, the visible length and the sharpness (in proximal 4-cm and full-visible course) of both the RCA and the combined LM + left anterior descending (LAD) coronary arteries were quantified using the Soap-Bubble software tool.[40] Because the visibility of the coronary arteries typically is very low in motion-degraded reconstructions from All Data, this analysis was only performed for SIMBA and FRF in vessels where both methods could visualize the ostia. Furthermore, an experienced pediatric cardiologist (K.K.W.) investigated whether the clinical questions that motivated the cardiac MR exams of the pediatric patients could be answered using the SIMBA and FRF images.

3.5 | Analysis of the SIMBA data selection

To study our second objective, the automatically selected data in SIMBA was characterized. The number of selected interleaves was ascertained, and the ratio with respect to the total number of interleaves was computed for each data set. Moreover, the uniformity of the 3D radial sampling in k-space was analyzed by examining the distribution of the selected readouts on the unit sphere. Specifically, the average great-circle distance between readouts and their four closest neighbors as well as the relative SD thereof were computed. This relative SD metric reflects how variable the distances between the k-space samples and their neighbors are, with a lower value corresponding to higher uniformity.[36] These two analyses were also performed for All Data and FRF.

We further examined the provenance of the interleaves selected by SIMBA relative to their cardiac phases and respiratory positions. In the cardiac dimension, the selected interleaves were categorized as either systolic or diastolic based on their associated ECG timestamps, corresponding to how long after an R-wave they were acquired. As a reference, individual systolic durations were obtained by approximating the QT interval

using an empirical formula,[21,41] and then subtracting an approximate R-wave peak time of 35 ms.[42] Based on this categorization, the average percentage of data that originated from the subject-specific diastolic interval was computed. Additionally, the SIMBA data selection was categorized as systolic, diastolic, or mixed for each subject. The vessel sharpness of the full LM + LAD and the full RCA was also evaluated for each of these categories separately for both SIMBA and FRF, and intracategory comparisons were reported. In the respiratory dimension, we investigated in which respiratory state the readouts selected by SIMBA were acquired. For that analysis, the respiratory self-gating signal from FRF[13] served as a subject-specific reference to sort all of the acquired imaging data into four different respiratory levels. For every subject, it was determined what percentage of data selected by SIMBA was contained in the two most end-expiratory bins, and whether most of the selected data originated from end-expiration, inspiration, or an intermediate state.

3.6 | Statistical analysis

For statistical comparisons of continuous variables, either two-sided paired sample t-tests or Wilcoxon signed-rank tests were used, depending on whether the variable appeared to be normally distributed or not. Jarque-Bera tests[43] were used for assessing normality. McNemar's tests were used for nominal variables. In all statistical testing, $P < .05$ was considered statistically significant. To correct for multiple comparisons, the Benjamini-Hochberg[44] procedure was used where applicable. For the analyses of image quality, separate analyses were performed for volunteers and patients. Elsewhere, both groups were considered together.

4 | RESULTS

4.1 | Image reconstruction

The SIMBA reconstruction allowed for fast 20-second reconstructions of 3D whole-heart images: principal component analysis, 0.6 ± 0.5 seconds; k-means clustering, 11.1 ± 4.8 seconds; and nonuniform fast Fourier transform and sum-of-squares coil combination, 7.5 ± 1.6 seconds. On the same computer, 36.7 ± 7.4 seconds were required only for the nonuniform fast Fourier transform and coil combination of All Data. The iterative FRF reconstructions took 2:47 ± 1:02 hours per subject, although it should be emphasized that those reconstructions generated 5D images with 32-96 (heart rate–dependent) different 3D volumes and were performed on a more powerful machine.

4.2 | Image quality

Visually, SIMBA suppressed most of the motion blur seen in the All Data reconstructions and provided comparable image quality to FRF (Figure 2). Both SIMBA and FRF provided significantly higher average blood–myocardium interface sharpness than All Data in volunteers and patients (all $P < .05$; Figure 3A). In volunteers, that interface was sharper with SIMBA than with FRF ($P < .001$). The average sharpness values in volunteers were 1.5 ± 0.2 for

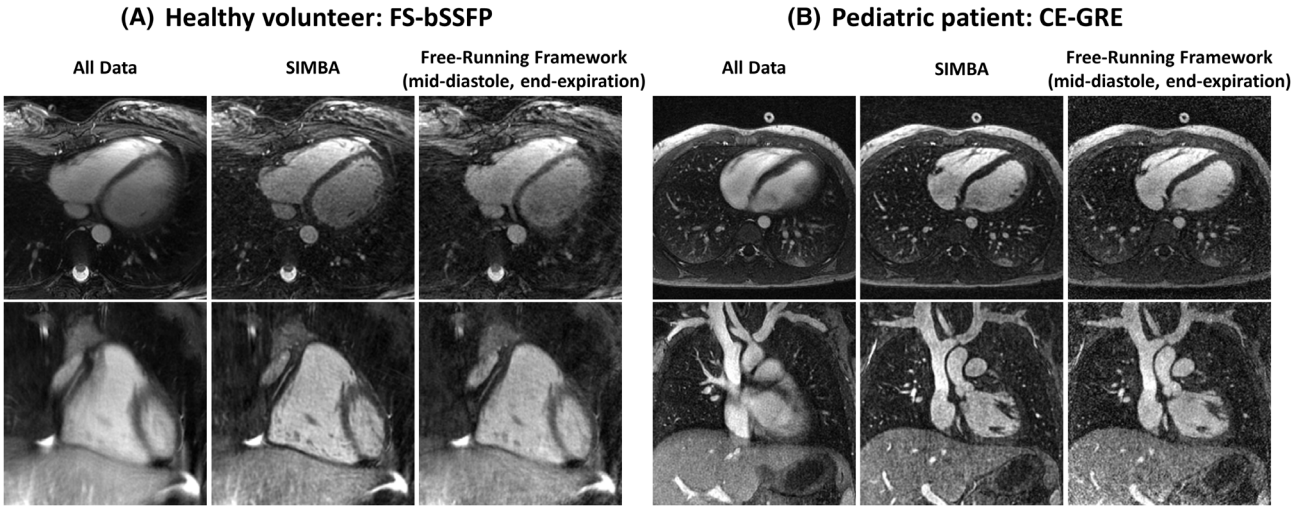

FIGURE 2 Representative examples of axial and coronal reformats at locations where the coronary arteries generally are visible, from one noncontrast fat saturated balanced SSFP (FS-bSSFP) scan of a healthy volunteer (A) and one ferumoxytol contrast-enhanced gradient echo (CE-GRE) scan of a pediatric cardiac patient (B). Both data sets were reconstructed with All Data (left columns), SIMBA (middle columns), and free-running framework (right columns). In general, the SIMBA images appear sharper and show less motion artifacts than their All Data counterparts. Moreover, the motion state selected by SIMBA matches that of the end-expiratory, middiastolic FRF images well

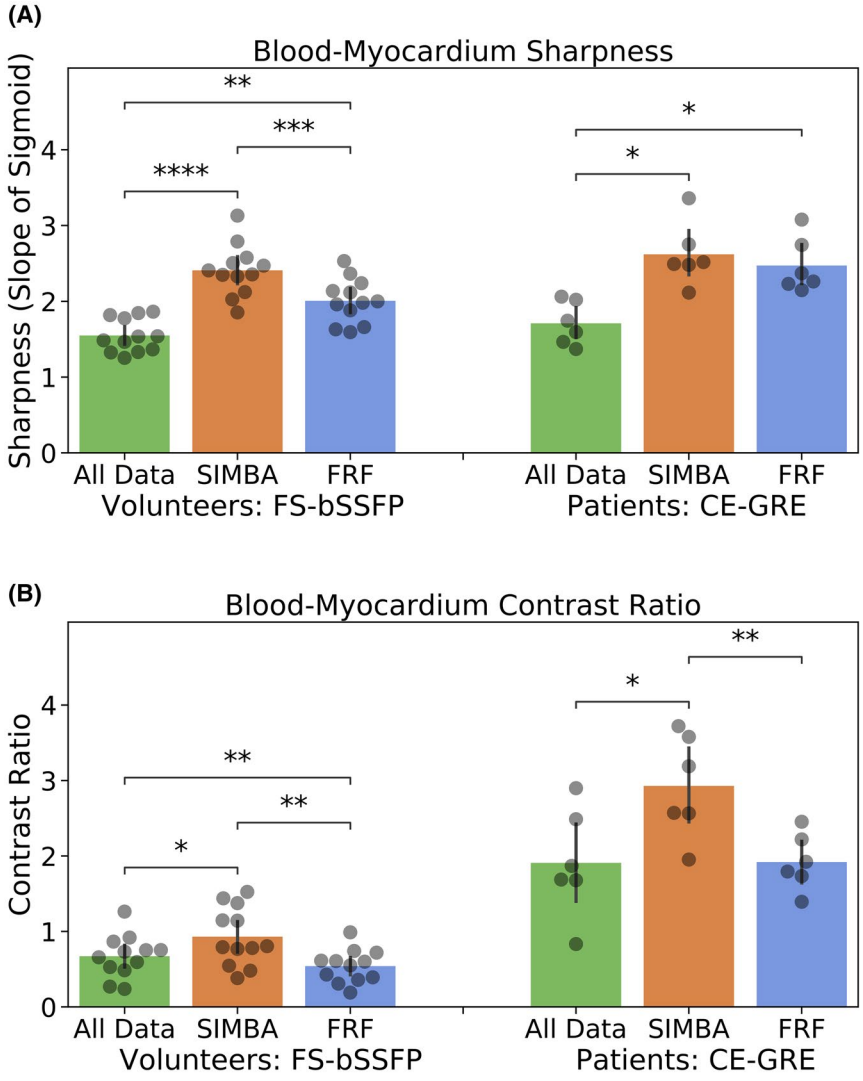

FIGURE 3 Blood–myocardium interface sharpness and contrast ratio. A, Bar plots with 95% confidence intervals showing the average blood–myocardium interface sharpness as quantified by fitting parametrized sigmoid functions to the interface and using the average slope parameter value as a measure of sharpness. Overall, SIMBA provided the images with the sharpest blood–myocardium interfaces, although without reaching statistical significance when compared with the free-running framework (FRF) in patients. B, Bar plots showing the average blood–myocardium contrast ratio. As expected, CE-GRE images had higher blood–myocardium contrast than the noncontrast FS-bSSFP images. The SIMBA images had the best blood–myocardium contrast both in volunteers and patients

All Data, 2.4 ± 0.3 for SIMBA, and 2.0 ± 0.3 for FRF. In patients, sharpness was measured as follows: 1.7 ± 0.3 for All Data, 2.6 ± 0.4 for SIMBA, and 2.5 ± 0.4 for FRF. The blood–myocardium contrast ratios in volunteers were 0.7 ± 0.3 for All Data, 0.9 ± 0.4 for SIMBA, and 0.5 ± 0.2 for FRF, and in patients they measured 1.9 ± 0.7 for All Data, 2.9 ± 0.7 for SIMBA, and 1.9 ± 0.4 for FRF (Figure 3B). The SIMBA reconstruction provided significantly higher contrast ratio than both All Data and FRF (all corrected $P < .05$). The All Data images had a higher blood SNR and blood–myocardium CNR than SIMBA in volunteers (SNR: 14.9 ± 6.3 and 7.2 ± 3.0, $P < .001$; and CNR: 5.9 ± 3.1 and 3.5 ± 1.9, respectively, $P < .001$) and patients (SNR: 27.8 ± 9.8 and 16.8 ± 6.0, $P < .01$; and CNR: 17.1 ± 5.2 and 12.5 ± 4.9, respectively, $P < .01$).

Significantly more coronary ostia were visible with both SIMBA and FRF compared with All Data (both $P < .001$; All Data, 4 of 36; SIMBA, 31 of 36; and FRF, 34 of 36). No significant difference was found between SIMBA *and* FRF ($P = .25$). The measurements of coronary artery visibility and sharpness are summarized in Table 2. Briefly, the average vessel sharpness of the RCA was lower with SIMBA compared to FRF, although a statistically significant difference only was found in the proximal vessel in the volunteer cohort ($P < .05$). No significant differences in LM + LAD sharpness and visible vessel length were measured. Examples of coronary artery reformats are provided in Figure 4. Moreover, SIMBA allowed for answering the clinical question with confidence in 5 of 6 patients, whereas the FRF did so in 6 of 6 (Supporting information Table S1).

TABLE 2 Assessment of the conspicuity of the coronary arteries

Metric	Data					
	FS-bSSFP volunteers: All Data	**FS-bSSFP volunteers: SIMBA**	**FS-bSSFP volunteers: FRF**	**CE-GRE patients: All Data**	**CE-GRE patients: SIMBA**	**CE-GRE patients: FRF**
Visible LM ostium (count)	0/12	**10/12**	**10/12**	2/6	**6/6**	**6/6**
Visible RCA ostium (count)	1/12	10/12	**12/12**	1/6	5/6	**6/6**
Analyses performed in the vessels with visible ostia for both SIMBA and FRF:						
Metric	**Data**					
	FS-bSSFP volunteers: SIMBA	**FS-bSSFP volunteers: FRF**	**Paired two-sided t-test *p*-value**	**CE-GRE patients: SIMBA**	**CE-GRE patients: FRF**	**Paired two-sided t-test *p*-value**
LM + LAD visibility (cm)	**8.1 ± 4.2**	6.4 ± 2.7	0.052	**6.3 ± 2.5**	5.9 ± 2.5	0.15
Proximal LM + LAD sharpness (%)	39.6 ± 7.5	**43.8 ± 8.8**	0.10	**46.9 ± 7.5**	41.5 ± 8.3	0.16
Full LM + LAD sharpness (%)	37.0 ± 7.6	**40.3 ± 8.2**	0.21	**44.1 ± 5.7**	39.2 ± 6.9	0.17
RCA visibility (cm)	8.3 ± 3.3	**9.2 ± 2.7**	0.18	6.2 ± 1.5	**6.4 ± 2.6**	0.82
Proximal RCA sharpness (%)	37.3 ± 9.2	**42.1 ± 10.5**[a]	0.049	34.9 ± 9.0	**39.0 ± 5.5**	0.37
Full RCA sharpness (%)	36.1 ± 8.1	**40.4 ± 8.9**	0.097	35.9 ± 7.7	**40.3 ± 6.1**	0.28

Note: Visibility and sharpness data are presented as mean ± SD. Bold text indicates highest mean/count.

[a]$P < .05$.

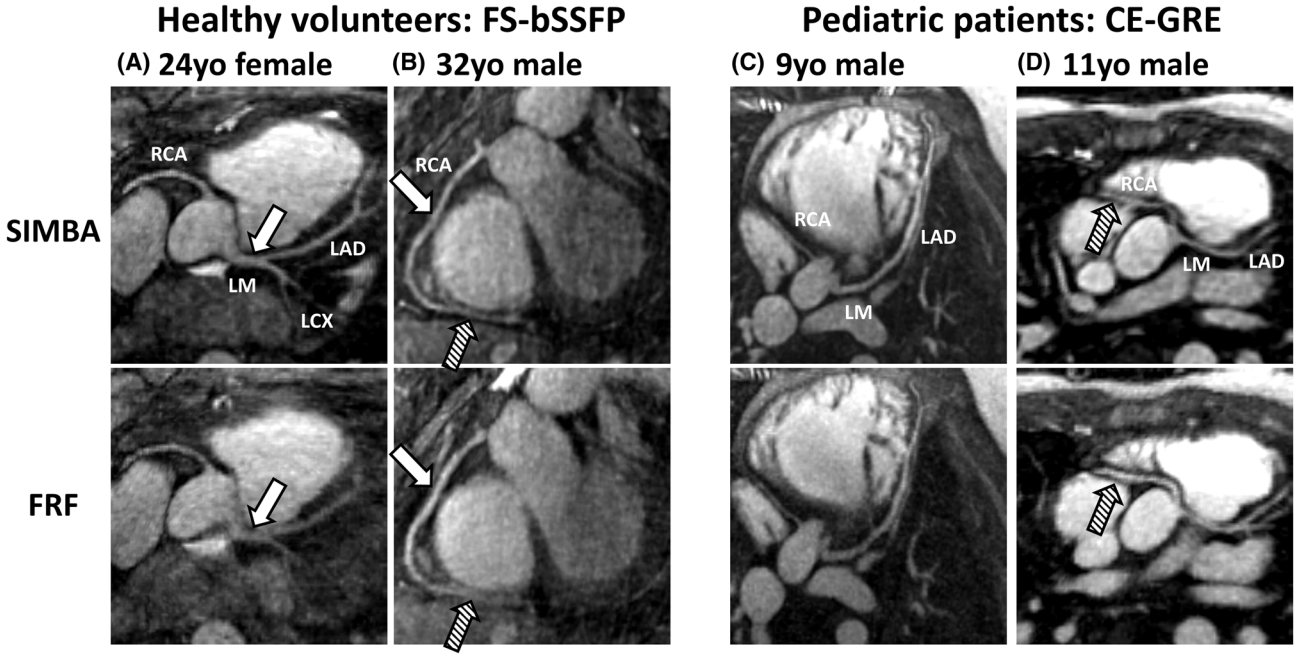

FIGURE 4 Examples of multiplanar reformats depicting coronary arteries from 4 different subjects. Overall, SIMBA and FRF images appeared relatively similar in terms of conspicuity of the coronary arteries. Although which of the two techniques that provided the best conspicuity varied between subjects, FRF tended to provide the sharpest right coronary arteries (RCAs). A, In this healthy volunteer, SIMBA visualized the left coronary tree more clearly (solid arrows). B, Here, FRF seemingly provided improved delineation of the proximal parts of the RCA (solid arrows), whereas SIMBA visualized the distal part better (striped arrows). C, In this patient, both the SIMBA and the FRF images allowed for ruling out the suspected left main (LM) dilation. D, The anomalous RCA, originating from the left coronary sinus, is seen in both image types. However, the proximal RCA appears sharper in the FRF image than in the SIMBA image (striped arrows), as corroborated by the corresponding quantitative measurements of vessel sharpness. Abbreviations: LAD, left anterior descending; LCX, left circumflex

4.3 | The SIMBA data selection

The cluster selected by SIMBA ($C_{largest}$) contained on average 14 964 ± 2111 readouts, which corresponded to 11.8 ± 1.7% of the acquired data and 25.8 ± 3.6% of the radial Nyquist limit.[45] Reformats from 1 subject and the corresponding reference data vectors are depicted in Figure 5. The average great-circle distance was $7.4{\cdot}10^{-3}$ for All Data, $1.8{\cdot}10^{-2} \pm 1.1{\cdot}10^{-3}$ for SIMBA, and $4.8{\cdot}10^{-2} \pm 6.7{\cdot}10^{-3}$ for FRF. This average distance was significantly smaller for SIMBA when compared with FRF ($P < .001$), but significantly higher when compared with All Data ($P < .001$). The data selected using SIMBA had a more uniform distribution in k-space than the more undersampled FRF frames, according to the relative SDs of 27.4 ± 3.1% and 29.9 ± 2.4%, respectively ($P < .001$). The oversampled All Data reconstructions (~215% Nyquist) showed the highest uniformity with a relative SD of 5.9% (both $P < .001$).

Regarding the physiological motion consistency of the SIMBA selection, on average 72 ± 22% of the selected data originated from diastole. Diastolic images were obtained in 8 of 18 subjects, systolic in 4 of 18, and a combination thereof in 6 of 18 (Figure 6A). This combination contained early systolic and diastolic data and did not appear to imply poor perceived image quality (see, for example, contrast-enhanced gradient-echo examples in Figures 2 and 5). However, in the subjects with such mixed cardiac selection, FRF provided significantly sharper RCAs than SIMBA ($P = .046$; Supporting information Table S2). No significant differences were found in RCA sharpness in the two groups with systolic and diastolic SIMBA data selection or in LM + LAD sharpness in any of the groups. Further investigations indicated that the mixed cardiac selection could result in slightly different contractile states of the heart being combined (Supporting information Figure S1) and that mixed selection could not be avoided by simply increasing the number of clusters (Supporting information Figure S2). In the pediatric patient with the highest heart rate, considerable cardiac motion blur was seen (Figure 7A). Regarding breathing motion, the selected cluster contained end-expiratory data in 14 of 18 subjects, inspiratory data in 2 of 18 subjects, and mixed data in 2 of 18 subjects (Figure 6B). On average, 78 ± 31% of the selected data were found in the two most end-expiratory FRF bins. In certain subjects with poor SIMBA image quality, the algorithm had selected nonexpiratory data (Figure 7B). Figure 8 shows images from 1 pediatric patient reconstructed from the data in different clusters. Interestingly, the clusters appear to correspond to different motion states.

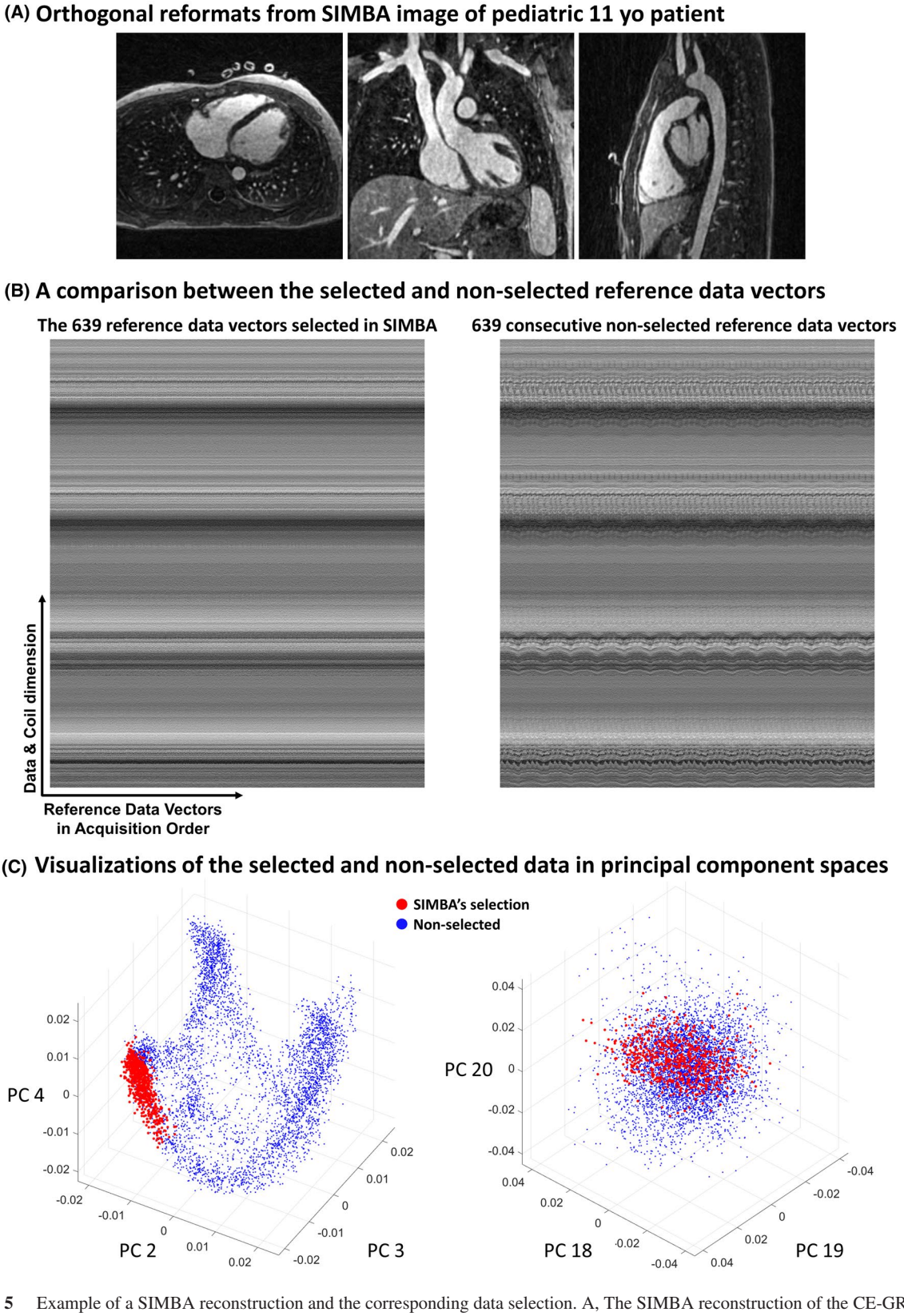

FIGURE 5 Example of a SIMBA reconstruction and the corresponding data selection. A, The SIMBA reconstruction of the CE-GRE scan of a pediatric patient. The visibility of the coronary arteries and the sharp lung–liver interface point toward a selection of motion-consistent data, in agreement with (B). B, Reference data vectors (stacked gradients of superior–inferior projections from four centrally located chest coil elements) of the interleaves in the selected most populated SIMBA cluster (left) and an equal amount of reference data vectors from consecutive, nonselected interleaves (right). The reference data vectors in the selected cluster show very little modulation by residual physiological motion, which suggests that the selected data have improved motion consistency. C, When plotting the reference data vectors of the selected interleaves in 3D spaces of different principal components (PCs), a general observation included a very clear discrimination between the selected (red) and the nonselected (blue) data in the lower principal component dimensions (left), whereas in the higher principal component dimensions, more mixing occurred (right)

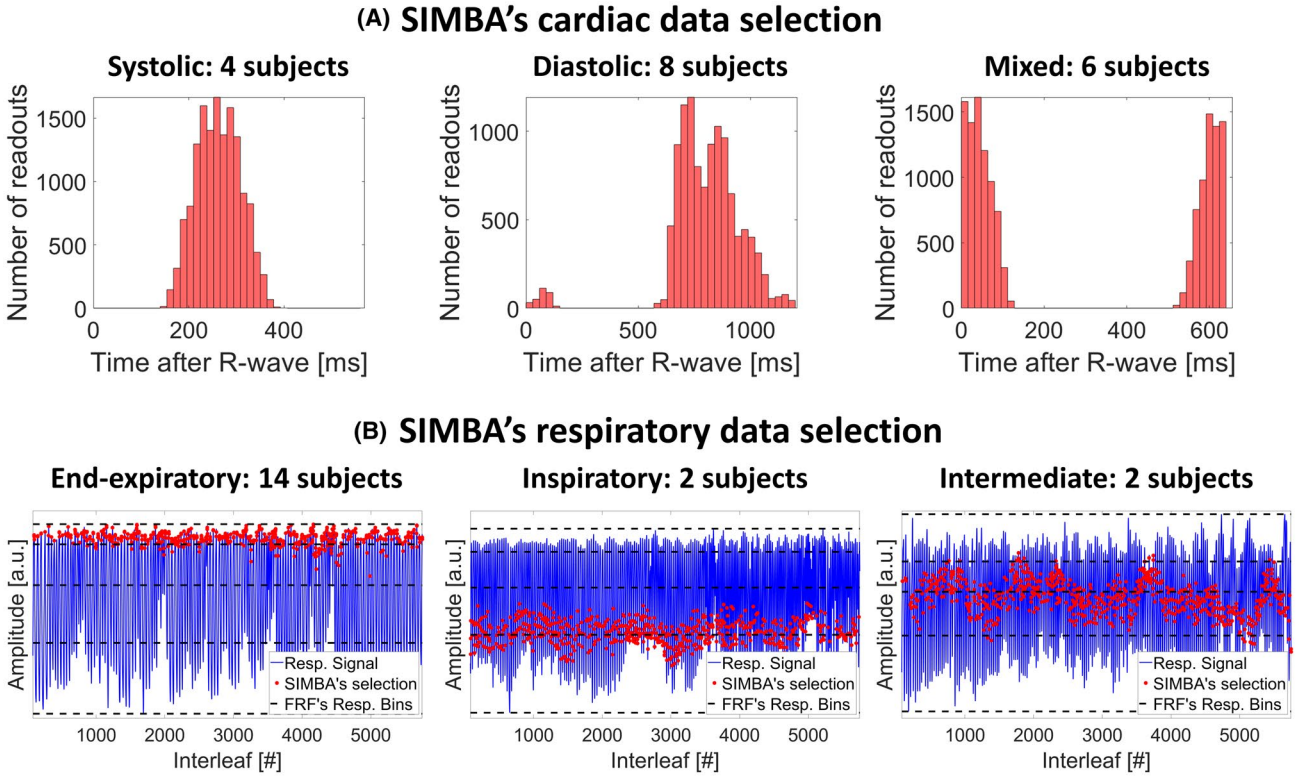

FIGURE 6 Physiological analysis of SIMBA's data selection. A, Three main cardiac data-selection scenarios occurred with SIMBA: systolic data (4 subjects), diastolic data (8 subjects), and a combination of early systolic and diastolic data (6 subjects). The latter is interesting, because the heart is likely to have a relatively similar shape during those two time points in the cardiac cycle, but it does not correspond to how data are usually selected using an ECG reference. The histograms correspond to SIMBA's cardiac data selection in 1 representative individual for each scenario. B, The SIMBA reconstruction primarily selected data from the most common respiratory state, end-expiration (14 subjects). In the 4 other subjects, data from inspiratory (2 subjects) or intermediate (2 subjects) respiratory positions were selected, which was associated with inferior image quality, consistent with the wider spread of the data points. For each of the identified respiratory SIMBA data-selection scenarios, the FRF respiratory self-gating signal (blue) with overlaid SIMBA selection (red) is displayed for a representative individual. The end-expiratory and end-inspiratory positions correspond to the highest and the lowest values on the y-axis, respectively

5 | DISCUSSION

This study aimed at developing and validating the SIMBA image-reconstruction technique that, when combined with free-running sequences, provides a simplified and fast solution for anatomical whole-heart MRA. The novelty of the proposed similarity-based method consists of automatically targeting an arbitrary subject-specific motion state, not making assumptions about the regularity and periodicity of the ongoing physiological processes, and not requiring the isolation of different motion sources from one another.

The findings that SIMBA images showed higher blood–myocardium sharpness and contrast ratio than the All Data images, and similar coronary vessel sharpness as FRF images, suggest that motion-suppressed whole-heart MRA can be obtained without making a priori physiological assumptions. Nonsignificant differences in sharpness between SIMBA and FRF might be explained by the fact that one SIMBA image, reconstructed without compressed sensing, contains more data than one FRF frame (~3% Nyquist), but FRF's regularization means that information is shared among frames. The finding that the fast-moving RCA was sharper in FRF images, although only significantly so in the proximal vessels of the volunteers, might be attributed to the temporal cardiac bin width of 50 ms, which was smaller than what was obtained with SIMBA (Figure 6A). The higher SNR and CNR in reconstructions with All Data compared with SIMBA might be a consequence of the considerably lower background noise in the oversampled All Data images. Additionally, SIMBA visualized more coronary ostia than All Data, which can be explained by more motion-consistent data. This is corroborated by the physiological analyses that showed how primarily end-expiratory data from limited portions of the cardiac cycle were selected.

Interestingly, nonevident ways of combining data from nonadjacent phases in the cardiac cycle were identified by SIMBA, as seen when early systolic and diastolic data clustered together (Figure 6A). This result is intuitively explained by large parts of the heart having a similar anatomical shape during those two phases of the cardiac cycle, although the

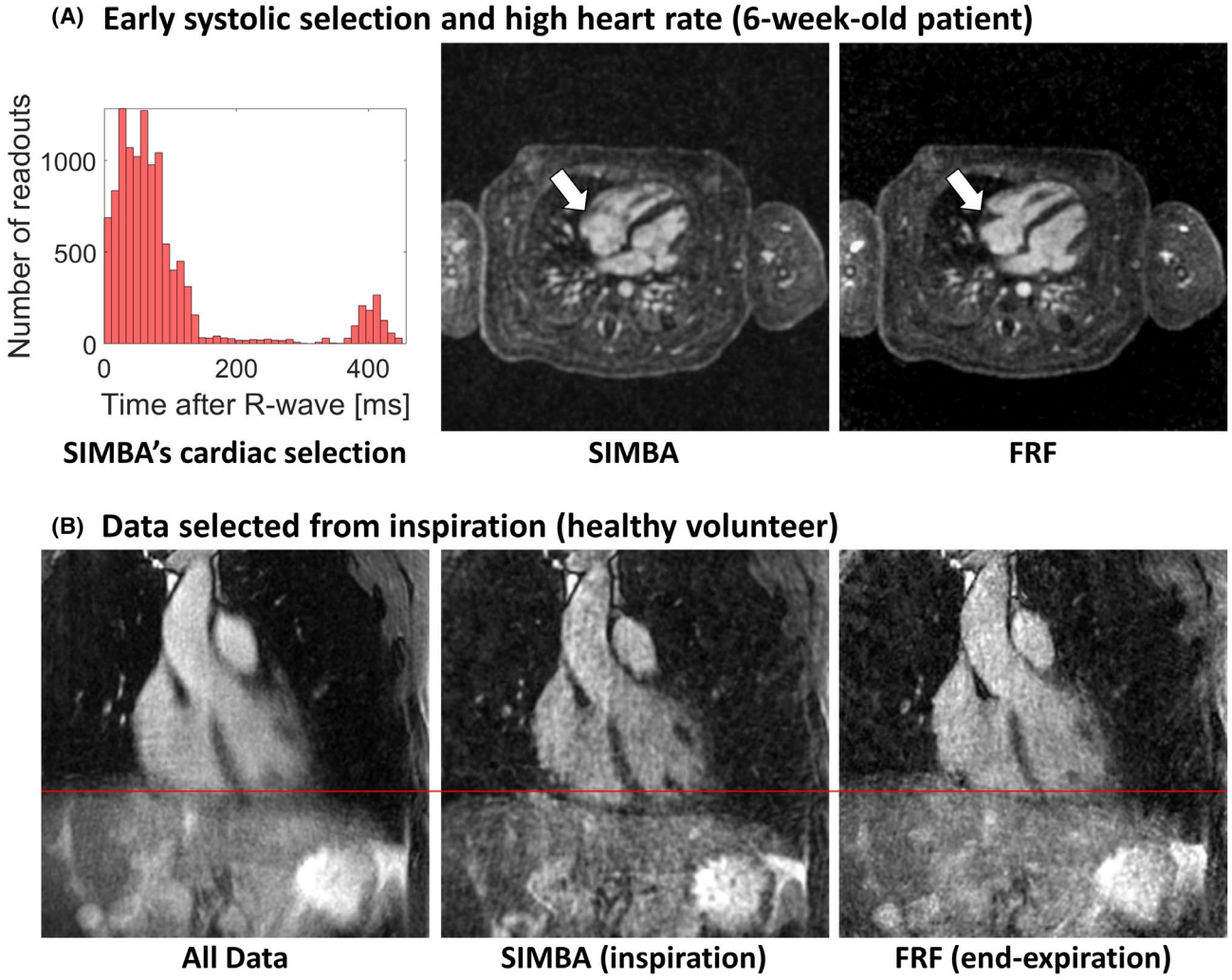

FIGURE 7 Examples of 2 subjects in whom SIMBA resulted in suboptimal image quality. A, In this 6-week-old infant, with a high average heart rate of 146 beats per minute, the image from the SIMBA reconstruction (middle) showed substantial residual cardiac motion artifacts. The atrioventricular groove (arrows) is considerably more blurred in the SIMBA image than in its FRF counterpart (right). The histogram on the left illustrates to which parts of the cardiac cycle the imaging data used in the SIMBA reconstruction corresponded. The large selection window in early systole most certainly means that data acquired both during the isovolumetric contraction and the rapid ejection phases of the cardiac cycle were used for the image reconstruction. This is a possible contributor to the cardiac-motion artifacts. B, A healthy volunteer with poor image quality. Using SIMBA, inspiratory data were selected (see the liver dome with respect to the red reference line, same subject as central respiratory signal in Figure 6B), which may have contributed to the overall blurriness. However, the end-expiratory FRF image was also of poor image quality for this individual

clustering might not be sensitive enough to small but important variations in, for example, the contractile state of the atria or the position of the valves. The finding that SIMBA provided significantly lower RCA sharpness than FRF in the group of subjects with mixed cardiac selection (Supporting information Table S2), but not in the groups with systolic or diastolic selection, suggests that such mixed data selection might be associated with motion blur. However, further investigations are warranted in a larger number of subjects for the different categories. In general, the blurriness of the heart, including lower RCA sharpness than for FRF, in some of the SIMBA reconstructions (Figure 7A) is likely a result of residual cardiac motion in the selected data. Another contributing factor, in addition to the mixed selection, is that data were clustered on an interleaf-by-interleaf basis. This may sometimes result in too long continuous portions of acquired data being used for reconstruction of the SIMBA image, thus leading to poor temporal resolution. To mitigate this issue, fewer readouts per interleaf could be acquired, potentially in combination with an increased number of clusters, to improve the motion consistency.

Although the acquisition time is similar to that of conventional ECG-triggered and navigator-gated whole-heart MRA sequences and the output remains a 3D image, there are important advantages of a free-running sequence with SIMBA reconstruction. These include there being no need

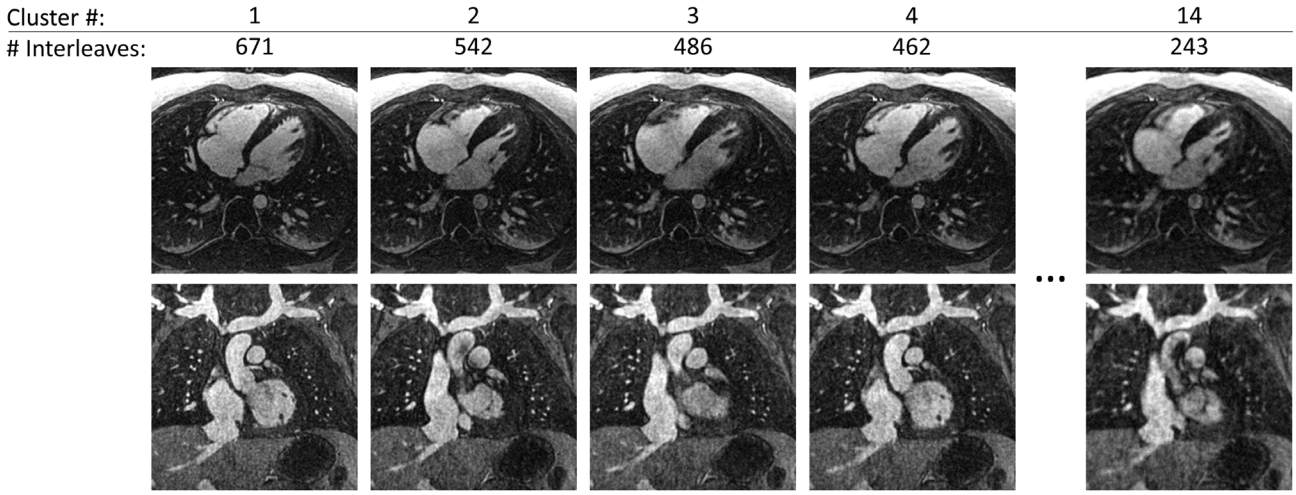

FIGURE 8 Images corresponding to SIMBA clusters sorted in descending order of number of interleaves for a 9-year-old male patient with ferumoxytol. Throughout this study, only the most populated of the SIMBA clusters identified for each subject was used for image reconstruction, analysis, and comparison. However, as exemplified here with axial and coronal reformats, reconstructions of additional, less-populated clusters may also provide informative images of high quality. The different clusters appear to correspond to different cardiac and respiratory motion states. Interestingly, in this case, it appears that the most populated cluster and the second-most-populated cluster correspond to diastolic and systolic images, respectively. In this work, a density compensation function that saturates at the Nyquist limit in k-space was used for the SIMBA reconstructions, which explains why the images from less-populated clusters show blurring instead of radial streaking artifacts

to place ECG leads, to carefully set up acquisition windows, nor to plan respiratory navigators. The SIMBA reconstruction might also be less sensitive to RR variability and respiratory drift, as no specific motion state is targeted, although this remains to be investigated. For the 6 pediatric patients in this study, successful visualization of the coronary ostia was crucial for answering the clinical questions at hand (Supporting information Table S1). In these subjects, SIMBA could visualize 11 of 12 (~92%) ostia and FRF could visualize 12 of 12 (100%). However, our study was neither designed nor powered to ascertain the success rate of coronary ostia visualization in patients using SIMBA. Using ECG-triggered sequences, there are several studies that report visualization rates of the coronary ostia close to 100% in congenital heart disease patients.[46-49] Thus, an important future study will be to compare the diagnostic confidence using SIMBA with that of more conventional methods. Some recent techniques that use continuous acquisitions for whole-heart imaging, including both prospective[50] and retrospective motion management,[12,13,17,18,51-54] have the important advantage over SIMBA in that they provide dynamic information. For example, the ferumoxytol-enhanced ROCK-MUSIC technique provides cardiac-resolved reconstructions and demonstrated excellent depiction of the proximal and middle segments of the coronary arteries in pediatric congenital heart-disease patients,[52] whereas the coronary ostia were successfully visualized in all 10 subjects reported in their study. However, these techniques typically necessitate physiological assumptions and relatively long reconstruction times, whereas SIMBA is data-driven and fast. Consequently, one possible workflow would be to readily display the SIMBA image at the scanner console for assessment of anatomy and planning of subsequent scans, while a motion-resolved FRF image is made available to the reader as soon as the longer reconstruction process has finished.

5.1 | Study limitations

An important limitation of this study is that the low statistical power associated with small sample sizes increases the risk of type 2 errors. This is particularly true for the patient cohort.

Although the SIMBA concept does not require specifying expected physiological frequencies, the periodicity of the cardiac and the respiratory motions ensures that there are enough motion-consistent data for performing reconstructions without motion correction. Also, avoiding modeling the underlying physiology means that extraction of prespecified systolic or diastolic images is not straightforward at this juncture.

There are also limitations in the data analysis. The coronary artery sharpness of SIMBA and FRF was compared only in the vessels where both methods could visualize the ostia, which does not take into account that FRF could visualize more coronary ostia overall. Additionally, all of the clinical questions in our patient cohort pertained to the coronary arteries, which is not the case for congenital heart-disease patients in general. However, if the fast-moving coronary

arteries are well depicted, this is likely to be true also for other vessels of interest.

5.2 | Future directions

Optimization of the type of reference data vectors, dimensionality reduction method, and clustering technique would most likely improve the resulting image quality. This may be further supported by coil sensitivity–weighted coil combination, parallel imaging, compressed sensing, and/or denoising. Instead of relying solely on the SI readouts, it may be possible to use information from all of the readouts in an interleaf for creating a reference data vector, such as by reconstructing a subimage.[27] Alternatively, the sampling rate of the reference data vectors could be increased by using center-of-k-space coefficients or an external Pilot Tone.[55] Moreover, *k*-means enforces spherical clusters that might be suboptimal, as the data distribution in the clustering space might reflect important physiological information. Improvements might also be achieved by weighting the data points within the selected cluster based on their similarity, discarding outliers,[56] or applying intracluster motion correction. Furthermore, the proposed implementation used only the data in the most populated cluster for image reconstruction. As illustrated in Figure 8, different clusters correspond to different motion states. Hence, exploiting spatial correlations with a motion-resolved XD-GRASP[37] approach might enhance the images and potentially provide dynamic information. Furthermore, the utility of the SIMBA technique in the assessment of native coronary artery disease should be explored in a future study. Finally, SIMBA might also be useful in other free-breathing applications, such as in abdominal or lung imaging.

6 | CONCLUSIONS

The SIMBA technique enabled fast data-driven reconstruction of whole-heart MRA from free-running acquisitions, with an image quality superior to All Data and similar to that of the more time-consuming, motion-resolved, FRF reconstruction. Overall, SIMBA images showed sharp anatomical features, including visible coronary arteries, from which it can be inferred that respiratory and cardiac motion artifacts could be successfully suppressed without requiring specific a priori assumptions related to physiology. The SIMBA reconstruction intrinsically tended to select data that originated from well-defined time points in the cardiac cycle at end-expiration, although mixing of similar but nonidentical motion states could occur, which warrants further investigation. The SIMBA technique allows for simplified whole-heart imaging, because it is computationally inexpensive and applicable to free-running acquisitions that do not require any gating, triggering, or complicated planning.

CONFLICT OF INTEREST

John Heerfordt's PhD studies are supported financially by Siemens Healthcare (Erlangen, Germany). Dr. Matthias Stuber receives nonmonetary research support from Siemens Healthcare (Erlangen, Germany). Dr. Davide Piccini is an employee of Siemens Healthcare (Lausanne, Switzerland). The other authors have no relevant conflicts of interest to declare.

DATA AVAILABILITY STATEMENT

Data can be made available upon request to the corresponding author.

ORCID

John Heerfordt https://orcid.org/0000-0002-6837-4733
Jessica A. M. Bastiaansen https://orcid.org/0000-0002-5485-1308
Lorenzo Di Sopra https://orcid.org/0000-0003-3426-9457
Christopher W. Roy https://orcid.org/0000-0002-3111-8840
Matthias Stuber https://orcid.org/0000-0001-9843-2028
Davide Piccini https://orcid.org/0000-0003-4663-3244

TWITTER

Davide Piccini @CVMR_Lausanne

REFERENCES

1. Valsangiacomo Buechel ER, Grosse-Wortmann L, Fratz S, et al. Indications for cardiovascular magnetic resonance in children with congenital and acquired heart disease: an expert consensus paper of the imaging working group of the AEPC and the cardiovascular magnetic resonance section of the EACVI. *Eur Heart J Cardiovasc Imaging*. 2015;16:281-297.
2. McConnell MV, Ganz P, Selwyn AP, Li W, Edelman RR, Manning WJ. Identification of anomalous coronary arteries and their anatomic course by magnetic resonance coronary angiography. *Circulation*. 1995;92:3158-3162.
3. Sørensen TS, Körperich H, Greil GF, et al. Operator-independent isotropic three-dimensional magnetic resonance imaging for morphology in congenital heart disease: a validation study. *Circulation*. 2004;110:163-169.
4. Sakuma H, Ichikawa Y, Chino S, Hirano T, Makino K, Takeda K. Detection of coronary artery stenosis with whole-heart coronary magnetic resonance angiography. *J Am Coll Cardiol*. 2006;48:1946-1950.
5. Di Leo G, Fisci E, Secchi F, et al. Diagnostic accuracy of magnetic resonance angiography for detection of coronary artery disease: a systematic review and meta-analysis. *Eur Radiol*. 2016;26:3706-3718.
6. Greil G, Tandon A, Silva Vieira M, Hussain T. 3D whole heart imaging for congenital heart disease. *Front Pediatr*. 2017;5:1-10.
7. Bilchick KC, Berger RD. Heart rate variability. *J Cardiovasc Electrophysiol*. 2006;17:691-694.

8. Runge VM, Clanton JA, Partain CL, James AE. Respiratory gating in magnetic resonance imaging at 0.5 Tesla. *Radiology*. 1984;151:521-523.
9. Oshinski JN, Hofland L, Mukundan S, Dixon TW, Parks WJ, Pettigrew RI. Two-dimensional coronary MR angiography without breath holding. *Radiology*. 1996;201:737-743.
10. Ehman RL, Felmlee JP. Adaptive technique for high-definition MR imaging of moving structures. *Radiology*. 1989;173:255-263.
11. Ishida M, Schuster A, Takase S, et al. Impact of an abdominal belt on breathing patterns and scan efficiency in whole-heart coronary magnetic resonance angiography: comparison between the UK and Japan. *J Cardiovasc Magn Reson*. 2011;13:71.
12. Pang J, Sharif B, Fan Z, et al. ECG and navigator-free four-dimensional whole-heart coronary MRA for simultaneous visualization of cardiac anatomy and function. *Magn Reson Med*. 2014;72:1208-1217.
13. Di Sopra L, Piccini D, Coppo S, Stuber M, Yerly J. An automated approach to fully self-gated free-running cardiac and respiratory motion-resolved 5D whole-heart MRI. *Magn Reson Med*. 2019;82:2118-2132.
14. Stehning C, Börnert P, Nehrke K, Eggers H, Stuber M. Free-breathing whole-heart coronary MRA with 3D radial SSFP and self-navigated image reconstruction. *Magn Reson Med*. 2005;54:476-480.
15. Henningsson M, Koken P, Stehning C, Razavi R, Prieto C, Botnar RM. Whole-heart coronary MR angiography with 2D self-navigated image reconstruction. *Magn Reson Med*. 2012;67:437-445.
16. Piccini D, Feng LI, Bonanno G, et al. Four-dimensional respiratory motion-resolved whole heart coronary MR angiography. *Magn Reson Med*. 2017;77:1473-1484.
17. Feng LI, Coppo S, Piccini D, et al. 5D whole-heart sparse MRI. *Magn Reson Med*. 2018;79:826-838.
18. Coppo S, Piccini D, Bonanno G, et al. Free-running 4D whole-heart self-navigated golden angle MRI: initial results. *Magn Reson Med*. 2015;74:1306-1316.
19. Gharib AM, Herzka DA, Ustun AO, et al. Coronary MR angiography at 3T during diastole and systole. *J Magn Reson Imaging*. 2007;26:921-926.
20. Ginami G, Bonanno G, Schwitter J, Stuber M, Piccini D. An iterative approach to respiratory self-navigated whole-heart coronary MRA significantly improves image quality in a preliminary patient study. *Magn Reson Med*. 2016;75:1594-1604.
21. Roes SD, Korosoglou G, Schär M, et al. Correction for heart rate variability during 3D whole heart MR coronary angiography. *J Magn Reson Imaging*. 2008;27:1046-1053.
22. Winkelmann S, Schaeffter T, Koehler T, Eggers H, Doessel O. An optimal radial profile order based on the golden ratio for time-resolved MRI. *IEEE Trans Med Imaging*. 2007;26:68-76.
23. Chan RW, Ramsay EA, Cunningham CH, Plewes DB. Temporal stability of adaptive 3D radial MRI using multidimensional golden means. *Magn Reson Med*. 2009;61:354-363.
24. Heerfordt J, Whitehead KK, Bastiaansen JAM, et al. Similarity-based angiography (SIMBA) for fast reconstruction of static whole-heart coronary MR images from free-running acquisitions. In: Proceedings of the ISMRM & SMRT Virtual Conference & Exhibition, 2020. Abstract 2141.
25. van Heeswijk RB, Bonanno G, Coppo S, Coristine A, Kober T, Stuber M. Motion compensation strategies in magnetic resonance imaging. *Crit Rev Biomed Eng*. 2012;40:99-119.
26. Larson AC, White RD, Laub G, McVeigh ER, Li D, Simonetti OP. Self-gated cardiac cine MRI. *Magn Reson Med*. 2004;51:93-102.
27. Hardy CJ, Zhao L, Zong X, Saranathan M, Yucel EK. Coronary MR angiography: respiratory motion correction with BACSPIN. *J Magn Reson Imaging*. 2003;17:170-176.
28. Assent I. Clustering high dimensional data. *Wiley Interdiscip Rev Data Min Knowl Discov*. 2012;2:340-350.
29. MacQueen J. Some methods for classification and analysis of multivariate observations. In: Proceedings of the Fifth Berkeley Symposium on Mathematical Statistics and Probability, Volume 1. Berkeley, CA: University of California Press; 1967. pp 281-296.
30. Arthur D, Vassilvitskii S. K-means++: the advantages of careful seeding. In: Proceedings of the Annual ACM-SIAM Symposium on Discrete Algorithms, Philadelphia, Pennsylvania, 2007. pp 1027-1035.
31. Piccini D, Littmann A, Nielles-Vallespin S, Zenge MO. Respiratory self-navigation for whole-heart bright-blood coronary MRI: methods for robust isolation and automatic segmentation of the blood pool. *Magn Reson Med*. 2012;68:571-579.
32. Piccini D, Monney P, Sierro C, et al. Respiratory self-navigated postcontrast whole-heart coronary MR angiography: initial experience in patients. *Radiology*. 2014;270:378-386.
33. Knoll F, Schwarzl A, Diwoky C, Sodickson DK. gpuNUFFT—an open source GPU library for 3D regridding with direct Matlab interface. In: Proceedings of the Joint Annual Meeting of ISMRM-ESMRMB, Milan, Italy, 2014. Abstract 4297.
34. Beatty PJ, Nishimura DG, Pauly JM. Rapid gridding reconstruction with a minimal oversampling ratio. *IEEE Trans Med Imaging*. 2005;24:799-808.
35. Prince MR, Zhang HL, Chabra SG, Jacobs P, Wang Y. A pilot investigation of new superparamagnetic iron oxide (ferumoxytol) as a contrast agent for cardiovascular MRI. *J Xray Sci Technol*. 2003;11:231-240.
36. Piccini D, Littmann A, Nielles-Vallespin S, Zenge MO. Spiral phyllotaxis: the natural way to construct a 3D radial trajectory in MRI. *Magn Reson Med*. 2011;66:1049-1056.
37. Feng L, Axel L, Chandarana H, Block KT, Sodickson DK, Otazo R. XD-GRASP: golden-angle radial MRI with reconstruction of extra motion-state dimensions using compressed sensing. *Magn Reson Med*. 2016;75:775-788.
38. Ahmad R, Ding Y, Simonetti OP. Edge sharpness assessment by parametric modeling: application to magnetic resonance imaging. *Concepts Magn Reson Part A Bridg Educ Res*. 2015;44:138-149.
39. Dietrich O, Raya JG, Reeder SB, Reiser MF, Schoenberg SO. Measurement of signal-to-noise ratios in MR images: influence of multichannel coils, parallel imaging, and reconstruction filters. *J Magn Reson Imaging*. 2007;26:375-385.
40. Etienne A, Botnar RM, Van Muiswinkel AMC, Boesiger P, Manning WJ, Stuber M. "Soap-Bubble" visualization and quantitative analysis of 3D coronary magnetic resonance angiograms. *Magn Reson Med*. 2002;48:658-666.
41. Ashman R. Normal duration of the Q-T interval. *Proc Soc Exp Biol Med*. 1939;40:150.
42. O'Neal WT, Qureshi WT, Nazarian S, et al. Electrocardiographic time to intrinsicoid deflection and heart failure: the multi-ethnic study of atherosclerosis. *Clin Cardiol*. 2016;39:531-536.
43. Jarque CM, Bera AK. A test for normality of observations and regression residuals. *Int Stat Rev/Rev Int Stat*. 1987;55:163-172.
44. Benjamini Y, Hochberg Y. Controlling the false discovery rate: a practical and powerful approach to multiple testing. *J R Stat Soc Ser B*. 1995;57:289-300.

45. Boada FE, Christensen JD, Gillen JS, Thulborn KR. Three-dimensional projection imaging with half the number of projections. *Magn Reson Med*. 1997;37:470-477.
46. Velasco Forte MN, Valverde I, Prabhu N, et al. Visualization of coronary arteries in paediatric patients using whole-heart coronary magnetic resonance angiography: comparison of image-navigation and the standard approach for respiratory motion compensation. *J Cardiovasc Magn Reson*. 2019;21:1-9.
47. Rajiah P, Setser RM, Desai MY, Flamm SD, Arruda JL. Utility of free-breathing, whole-heart, three-dimensional magnetic resonance imaging in the assessment of coronary anatomy for congenital heart disease. *Pediatr Cardiol*. 2011;32:418-425.
48. Monney P, Piccini D, Rutz T, et al. Single centre experience of the application of self navigated 3D whole heart cardiovascular magnetic resonance for the assessment of cardiac anatomy in congenital heart disease. *J Cardiovasc Magn Reson*. 2015;17:55.
49. Albrecht MH, Varga-Szemes A, Schoepf UJ, et al. Diagnostic accuracy of noncontrast self-navigated free-breathing MR angiography versus CT angiography: a prospective study in pediatric patients with suspected anomalous coronary arteries. *Acad Radiol*. 2019;26:1309-1317.
50. Moghari MH, Barthur A, Amaral ME, Geva T, Powell AJ. Free-breathing whole-heart 3D cine magnetic resonance imaging with prospective respiratory motion compensation. *Magn Reson Med*. 2018;80:181-189.
51. Bastiaansen JAM, Piccini D, Di Sopra L, et al. Natively fat-suppressed 5D whole-heart MRI with a radial free-running fast-interrupted steady-state (FISS) sequence at 1.5T and 3T. *Magn Reson Med*. 2020;83:45-55.
52. Han F, Zhou Z, Han E, et al. Self-gated 4D multiphase, steady-state imaging with contrast enhancement (MUSIC) using rotating Cartesian K-space (ROCK): validation in children with congenital heart disease. *Magn Reson Med*. 2017;78:472-483.
53. Masala N, Bastiaansen JAM, Di Sopra L, et al. Free-running 5D coronary MR angiography at 1.5T using LIBRE water excitation pulses. *Magn Reson Med*. 2020;84:1470-1485.
54. Küstner T, Bustin A, Jaubert O, et al. Fully self-gated free-running 3D Cartesian cardiac CINE with isotropic whole-heart coverage in less than 2 min. *NMR Biomed*. 2021;34:e4409.
55. Vahle T, Bacher M, Rigie D, et al. Respiratory motion detection and correction for MR using the pilot tone: applications for MR and simultaneous PET/MR examinations. *Invest Radiol*. 2020;55:153-159.
56. Chaptinel J, Piccini D, Bonanno G, et al. Respiratory optimized data selection for more resilient self-navigated whole-heart coronary MR angiography. *Magn Reson Mater Phys Biol Med*. 2016;30:215-225.

SUPPORTING INFORMATION

Additional Supporting Information may be found online in the Supporting Information section.

FIGURE S1 Investigation of mixed cardiac selection. For 1 of the subjects in whom similarity-driven multidimensional binning algorithm (SIMBA) provided a mixed systolic and diastolic cardiac data selection, a motion-resolved XD-GRASP reconstruction was performed to examine the similarity of the systolic and diastolic images from the concerned parts of the cardiac cycle. The XD-GRASP reconstruction was performed with total-variation regularization along the respiratory dimension but without regularization along the cardiac dimension, to reduce the influence of information from other time points. It appears that the early systolic XD-GRASP image (red), the diastolic XD-GRASP image (yellow), and the SIMBA image (blue) are anatomically similar, but not identical. The difference image corresponds to the subtraction of the diastolic image from the systolic image

FIGURE S2 The SIMBA reconstructions with varying numbers of clusters (most populated cluster reconstructed). In 1 volunteer, it was investigated how the images and the cardiac data selection changed with an increasing number of clusters (k). It was found that data selection both in systole and diastole occurred independently of the number of clusters (see histograms with cardiac selection). This suggests that SIMBA might be insensitive to subtle differences in the anatomical motion state. The different anatomical motion state in the reconstruction with 40 clusters, compared to those with 14, 20, and 30 clusters, is explained by the data being extracted from slightly different time points in the cardiac cycle. Moreover, a density-compensation function that saturates at the Nyquist limit in k-space was used, which explains the higher numbers of clusters resulted in a loss of image details rather than significant undersampling artifacts

TABLE S1 Summary of the clinical indications for cardiac MR for the 6 pediatric patients and the cardiologist's comments regarding whether the image quality of the SIMBA and free-running framework reconstructions sufficed for answering the clinical question at hand. Note: The reader was not blinded to the reconstruction type. Abbreviation: FRF, free-running framework

TABLE S2 Vessel sharpness for different categories of cardiac SIMBA selection. Note: Because the vessel sharpness was quantified only in vessels with visible ostia for both SIMBA and FRF, only those vessels were included in this analysis. The sharpness was quantified along the full visible course of the vessel.

How to cite this article: Heerfordt J, Whitehead KK, Bastiaansen JAM, et al. Similarity-driven multi-dimensional binning algorithm (SIMBA) for free-running motion-suppressed whole-heart MRA. *Magn Reson Med*. 2021;86:213–229. https://doi.org/10.1002/mrm.28713